



The narrowing of dendrite branches across nodes follows a well-defined scaling law

Maijia Liao^a , Xin Liang^b, and Jonathon Howard^{a,1} 

^aDepartment of Molecular Biophysics and Biochemistry, Yale University, New Haven, CT 06520; and ^bTsinghua-Peking Joint Center for Life Sciences, School of Life Sciences, Tsinghua University, 100084 Beijing, China

Edited by Yuh Nung Jan, Howard Hughes Medical Institute, University of California San Francisco, San Francisco, CA, and approved May 17, 2021 (received for review October 28, 2020)

The systematic variation of diameters in branched networks has tantalized biologists since the discovery of da Vinci's rule for trees. Da Vinci's rule can be formulated as a power law with exponent two: The square of the mother branch's diameter is equal to the sum of the squares of those of the daughters. Power laws, with different exponents, have been proposed for branching in circulatory systems (Murray's law with exponent 3) and in neurons (Rall's law with exponent 3/2). The laws have been derived theoretically, based on optimality arguments, but, for the most part, have not been tested rigorously. Using superresolution methods to measure the diameters of dendrites in highly branched *Drosophila* class IV sensory neurons, we have found that these types of power laws do not hold. In their place, we have discovered a different diameter-scaling law: The cross-sectional area is proportional to the number of dendrite tips supported by the branch plus a constant, corresponding to a minimum diameter of the terminal dendrites. The area proportionality accords with a requirement for microtubules to transport materials and nutrients for dendrite tip growth. The minimum diameter may be set by the force, on the order of a few piconewtons, required to bend membrane into the highly curved surfaces of terminal dendrites. Because the observed scaling differs from Rall's law, we propose that cell biological constraints, such as intracellular transport and protrusive forces generated by the cytoskeleton, are important in determining the branched morphology of these cells.

allometry | microtubule transport | optimality | biological networks

Branched networks are ubiquitous in nature, ranging in size from watercourses and trees to cellular organelles and the cytoskeleton (1–6). Often, branch diameters change systematically throughout the network, with proximal branches thicker than distal ones. This variation is usually interpreted as an adaptation to, or consequence of, the flow of materials and/or information through the network (7, 8). To describe the changes in diameter over branch points, allometric (or scaling) relations of the form

$$d_m^p = d_{d1}^p + d_{d2}^p, \quad [1]$$

have been proposed, based mainly on theoretical arguments (see below), where $d_m(d_{d1}, d_{d2})$ is the mother (daughters) diameter (definitions in *SI Appendix*, Fig. S1) and p is the exponent. Among the most well-known laws are da Vinci's rule for trees ($p = 2$) (9), Murray's law for vascular and pulmonary systems ($p = 3$) (7), and Rall's law for neuronal processes ($p = 3/2$) (10). In this work, we ask whether neuronal dendrites obey these or other scaling laws.

Scaling laws have been derived theoretically using optimality arguments. For example, Murray's law for the vasculature minimizes the frictional dissipation associated with moving fluid through pipes, given a fixed volume of blood (7). Rall's law minimizes the propagation time of action potentials (11) and the decrement of graded electrical signals across dendrite branch points (12) (*SI Appendix*); it assumes that the density of ion channels is constant, and the cost of building or maintaining the surface area of the dendrite is

minimized. Da Vinci's law has been reformulated as the “pipe model” for plants, in which a fixed cross-section of stems and branches is required to support each unit amount of leaves (13). Experimental support for scaling laws, however, is scarce because of the difficulties of imaging entire branched networks and because intrinsic anatomical variability may obscure precise laws (14). Thus, it is an open question whether scaling laws such as Eq. 1 apply in biological systems.

To quantitatively test diameter-scaling laws in neurons, it is necessary to study cells in which all the dendrite diameters can be measured. This criterion is satisfied by *Drosophila* larval class IV dendrite arborization neurons, which serve as a model system for studying dendrite morphogenesis (15). These neurons, which have up to 2,000 branches, form an approximately planar network array (16) that tiles the external surface of the larvae like chain mail (17) (Fig. 1*A* and *B*) and function as sensory receptors of nociceptive (18) and proprioceptive (19) inputs. They can be marked with a GFP-tagged membrane protein expressed under a cell-specific promoter (20). We developed a superresolution method to measure even the finest dendrite diameters in these cells and have discovered a diameter-scaling law that differs from Eq. 1 and that holds throughout development.

Results

Dendrite Branch Diameters Are Precisely Measured Using a Superresolution Method. To test scaling laws, accurate measurements of dendrite branch diameters in class IV dendrites are essential. Conventional

Significance

To study the systematic variation of dendrite diameters, we established a superresolution method that allows us to resolve dendrite diameters in *Drosophila* class IV dendritic arborization neurons, a model cell for studying branching morphogenesis. Interestingly, the diameters do not follow any of the known scaling laws. We propose a different scaling law that follows from two concepts: Terminal branches have the smallest diameters, whose average is about 230 nm, and there is an incremental increase in cross-sectional area needed to support each additional terminal branch. The law is consistent with the growing dendritic tips making the primary metabolic demand, which is supplied by microtubule-based transport. If the law generalizes to other neurons, it may facilitate segmentation in connectomic studies.

Author contributions: M.L., X.L., and J.H. designed research; M.L. and X.L. performed research; M.L. and J.H. analyzed data; and M.L. and J.H. wrote the paper.

The authors declare no competing interest.

This article is a PNAS Direct Submission.

This open access article is distributed under [Creative Commons Attribution-NonCommercial-NoDerivatives License 4.0 \(CC BY-NC-ND\)](https://creativecommons.org/licenses/by-nc-nd/4.0/).

¹To whom correspondence may be addressed. Email: joe.howard@yale.edu.

This article contains supporting information online at <https://www.pnas.org/lookup/suppl/doi:10.1073/pnas.2022395118/-DCSupplemental>.

Published July 2, 2021.

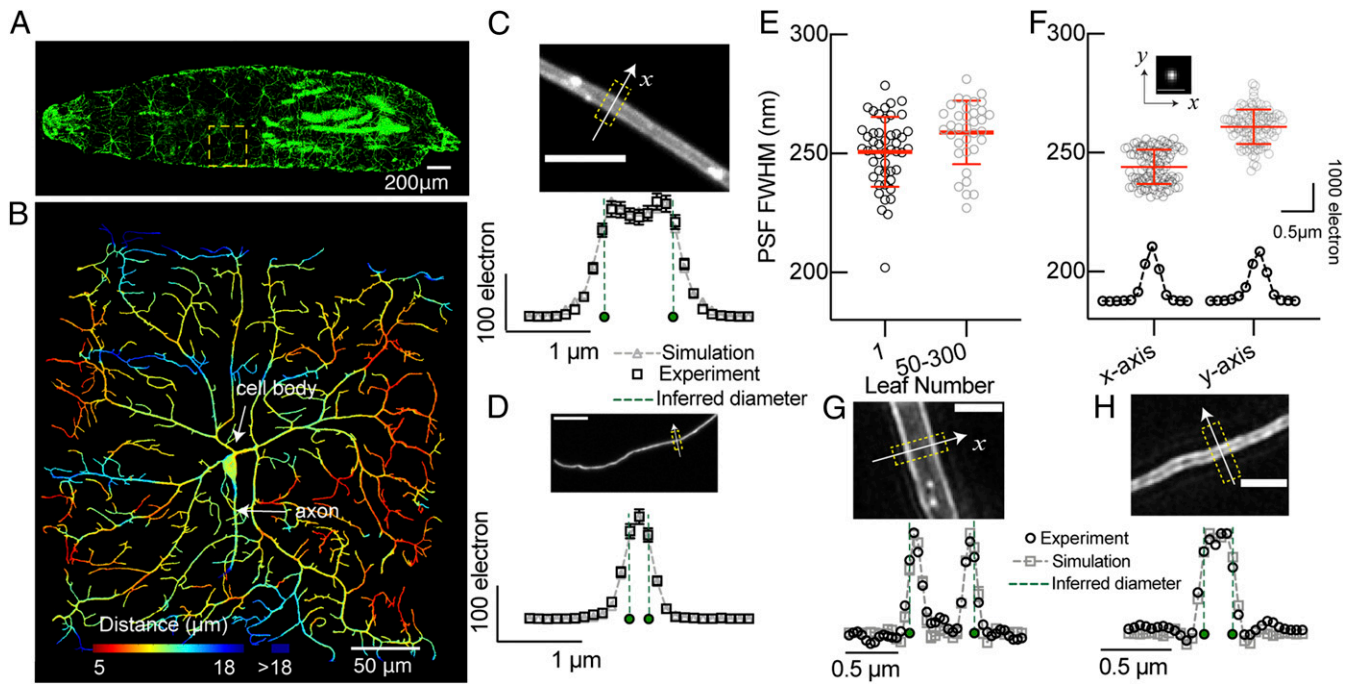


Fig. 1. Measurements of dendrite branch diameters by SDC and SIM. (A) Third-instar larva expressing GFP in its class IV neurons. One cell in abdominal segment 3 (A3) is boxed. Anterior is left. (B) Maximum projection image of a class IV neuron from the A3 segment constructed from 76 stacks (separated by 0.2 μm) from a SDC microscope (Nikon spinning disk, 50- μm pinholes, 40 \times water-immersion objective, NA = 1.25) of a 92-h after-egg-lay larva (*Shit^{ts1};ppkCD4-tdGFP*). The distance of the dendrites from the coverslip is color-coded: The cells are mostly within a depth of $\sim 12\ \mu\text{m}$, about 4% of their width. This dendritic tree has three arbors emerging from its cell body. (C and D) Maximum-intensity-projection images of a thick dendrite with leaf number 277 (C) and a terminal dendrite with leaf number 1 (D) from two ~ 132 -h larvae expressing tdGFP (60 \times water-immersion objective, NA = 1.2). The yellow boxes with width 1.1 μm indicate the regions of the dendrite where the intensity profiles of the middle section of the confocal stacks are shown below the images. Electron numbers are calculated based on sCMOS camera sensitivity. Black squares are experimental measurements (the SEs based on photon shot noise are mostly smaller than the markers). Gray triangles are simulations (the SEs based on 60 simulations are mostly smaller than the markers). The FWHMs from the PSF fits are $260 \pm 8\ \text{nm}$ in C and $266 \pm 34\ \text{nm}$ in D ($n = 6$ fits, mean \pm SD). The inferred diameters are $815 \pm 13\ \text{nm}$ in C and $231 \pm 29\ \text{nm}$ in D ($n = 6$ fits, mean \pm SE). (Scale bars, 5 μm .) (E) FWHM of PSF obtained from dendrites with different leaf numbers. Mean and SD are $251 \pm 15\ \text{nm}$ ($n = 48$ branches) for leaf no. 1 and $259 \pm 13\ \text{nm}$ ($n = 35$) for leaf no. 50–300. Red lines are mean and SD. Data are from two 132-h larvae. (F) PSF FWHMs of 100-nm-diameter tetra-speck beads (Upper Inset) measured from intensity profiles along the x axis and y axis (Lower Inset). Dashed fitting curves were generated from convolution of 100-nm beads with PSF. Mean and SD of the PSF FWHMs are $244 \pm 7\ \text{nm}$ ($n = 99$) and $261 \pm 7\ \text{nm}$ ($n = 99$). Red lines are mean and SD. The PSF FWHMs of the examples profiles are 239 nm (x axis) and 263 nm (y axis), respectively. (Scale bar, 1 μm .) (G and H) Maximum intensity projections of deconvolved SIM image of a thicker (G) and a thinner dendrite (H). Curve-fitting gave inferred diameters of $610 \pm 24\ \text{nm}$ and $200 \pm 9.2\ \text{nm}$ (mean \pm SD, $n = 6$) and inferred FWHMs of the PSF of $106 \pm 5.3\ \text{nm}$ and $109 \pm 5.3\ \text{nm}$ (mean \pm SD, $n = 6$). (Scale bars, 1 μm .)

image-analysis techniques based on thresholding techniques (14, 21, 22) cannot resolve the diameters of the finest dendrites ($<300\ \text{nm}$). To accurately measure dendrite diameters, we developed a superresolution method that uses Monte Carlo (MC) optimization to fit simulated images (SI Appendix, Fig. S2 and Materials and Methods) to experimental images obtained by spinning-disk confocal (SDC) microscopy (Fig. 1 C and D). The simulated images are model dendrites (hollow cylinders with uniformly distributed fluorophores on their surfaces) convolved with the point-spread function (PSF) of the confocal microscope. The experimental images are z stacks. The principle behind the method is that even for the thinnest dendrites, a best fit to the experimental data is obtained by using a cylinder of nonzero diameter (i.e., the cylinder gives a better fit to the data than a line). Even though the lateral resolution for the confocal microscope is $\sim 200\ \text{nm}$ (full-width at half-maximum [FWHM] $\approx 0.5\lambda/\text{numerical aperture [NA]}$, where NA = 1.2 is the NA of the water-immersion objective and $\lambda \approx 520\ \text{nm}$ is the emission wavelength), the method can resolve the diameters of synthetic images (simulated images with added noise; SI Appendix, Fig. S2) below 150 nm (Table 1), which is less than the diameter of the finest dendrites in these cells.

Our simulations provide good fits to the intensity profiles of thick class IV dendrites (Fig. 1C), which have two peaks with a

dip in the middle. This shows that a cylinder is a good model for the dendrite. Further validation of the model comes from the inferred FWHM of the PSF (Fig. 1E, right), which is in good agreement with that measured by using tetra-speck beads (Fig. 1F). Thus, the thicker dendrites serve as an in vivo calibration of the PSF. The profiles of the terminal dendrites do not show a dip (Fig. 1D). Nevertheless, the fitting gave an optimal FWHM of the PSF that was in good agreement with that of the thicker dendrites (Fig. 1E). This shows that the fitting procedure is robust and that the inferred diameters are reliable.

Dendrite Branch Diameters Do Not Obey Known Scaling Laws. Before testing scaling laws, we first confirmed that dendrite branches have well-defined diameters. We imaged one to three arbors of dendritic trees from six fully developed third-instar larvae ($\sim 132\ \text{h}$ after the time the egg was laid; egg lay was defined as time zero). We measured diameters using the superresolution method at three positions along 306 branches from the six larvae, avoiding locations where the membrane bulged due to the presence of membrane-bounded organelles. We measured the normalized diameter and the normalized displacement along the branch, where zero displacement is toward the cell body (definitions in Fig. 24). The diameter decreased only slightly along the length: the slope was -2.3% ,

Table 1. Accuracies of diameter measurements

Cylinder properties	Diameters (nm)				
Synthetic images (ground truth)	144	216	432	648	864
Inferred diameters, mean \pm SD	140 \pm 25	222 \pm 16	422 \pm 24	659 \pm 22	880 \pm 19

The superresolution method was applied to synthetic images (which included photon shot noise) with model diameters in the top row (*SI Appendix*, Fig. S2). The inferred diameters after fitting the simulated images to the synthetic images are in good agreement with the model diameters. $n = 18$ simulations.

much smaller than the average diameter change from the proximal, mother branch (-18%) and to the distal, daughter branches (-11%) (Fig. 2B). Thus, branch segments do not taper appreciably, and diameters change primarily across branch nodes.

To test the scaling law of Eq. 1, we calculated the exponents, p , for 253 branch points in six cells from the six 132-h larvae that were used in Fig. 2B. These branch points sampled the full range of branch orders. The mean exponent of 7.2 (Fig. 2C) does not support any of the aforementioned scaling laws (i.e., Rall, da Vinci, and Murray). Furthermore, the wide range of exponents ($SD = 8.8$) is not consistent with any specific scaling law. Alternative allometric relations are therefore required.

The Systematic Change of Dendrite Diameters Can Be Described by an Alternative Scaling Law. Among a wide range of allometric relations that we tested, we discovered an approximately linear relationship between the leaf number, n , of a branch (n is defined as the number of tips that the branch supports; Fig. 3A and *SI Appendix*, Fig. S3) and the branch's cross-sectional area (A): $A = \beta n + A_0$, where β is the slope and A_0 is the y intercept (Fig. 3B). Because the leaf number in a bifurcating network satisfies the simple allometric relation $n_m = n_{d1} + n_{d2}$, where n_m (n_{d1} , n_{d2}) is the leaf numbers of the mother (daughters), the linear relationship implies an alternative allometric scaling law:

$$d_m^2 + d_0^2 = d_{d1}^2 + d_{d2}^2, \quad [2]$$

where $d_0^2 = 4A_0/\pi$ (see *SI Appendix* for derivation). A nonzero intercept A_0 implies that there is a minimum dendrite diameter: The terminal branch with one tip has a diameter $d_1 = (d_0^2 + 4\beta/\pi)^{1/2}$.

To test whether the exponent equals two, which corresponds to cross-sectional area, is the most appropriate, we fit the experimental data from the six 132-h larvae to $d^p = \bar{p}n + d_0^p$. This scaling law provided a good fit (Fig. 3C), and the exponent p was narrowly distributed with an average of 1.97, close to that for the cross-

sectional area (Fig. 3D). Thus, our modified scaling law with a minimum diameter and an area dependence provides a good description of diameter scaling in class IV dendrites.

Minimum Diameter. A minimum diameter is well supported by the data. First, the y intercept in Fig. 3B is significantly greater than zero ($p \ll 0.005$, Student's t test using the mean and SE in the Fig. 3 legend). And second, the intensities of the terminal branches are similar to those of their mothers (Fig. 3E and F), consistent with terminal branches (leaf no. 1) having similar diameters to their mothers (leaf no. 2). If there were no minimum diameter and the scaling law with exponent two continued across the most distal branch point, we would expect the daughter intensity to be $1/\sqrt{2} \cong 70\%$ that of the mother (dashed line in Fig. 3F). However, the measured intensities of the terminal branches are close to those of their mothers: $93\% \pm 13\%$ (mean \pm SD, $n = 20$; Fig. 3F). Note that if there were less transport of fluorescent protein into the distal branch, we would expect a further reduction in intensity below 70%, contrary to what was observed. Thus, the minimum diameter in the scaling law is well supported experimentally. The small scatter in the diameter measurements from the SDC images, with a coefficient of variation of $0.14 \cong 0.13/0.9$, confirms that the precision of the diameter measurement using this method is high.

The minimum diameter deduced by using our superresolution method from the SDC images was 231 ± 29 nm (mean \pm SD, $n = 81$). To provide an independent estimate of dendrite diameters, we imaged third-instar larvae using structured illumination microscopy (SIM; *Materials and Methods*). Because SIM has roughly twice the resolution of the SDC, the edges of the dendrites are resolved, even for some terminal ones (Fig. 1G and H). The average diameters of the terminal dendrites in third-instar class IV cells inferred from the SIM images (*Materials and Methods* and *SI Appendix*, Fig. S4) were 195 ± 38 nm (mean \pm SD, $n = 17$), similar to those measured from the SDC images (231 ± 29 nm, mean \pm SD, $n = 81$). The terminal diameters ranged from 158 to 297 nm (SDC) and 140 to 287 nm (SIM) (*SI Appendix*, Fig. S5). This

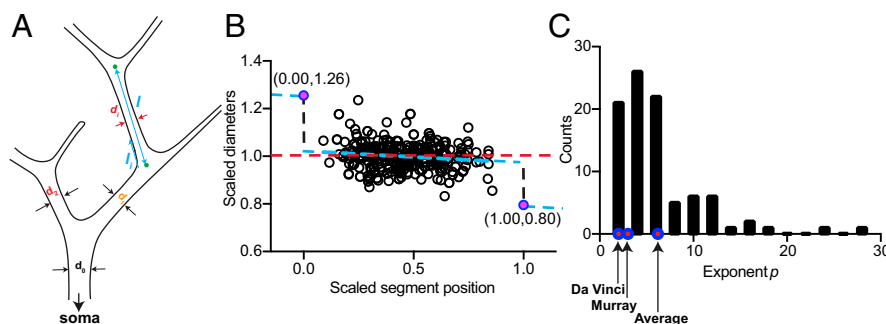


Fig. 2. Dendrite branch diameters do not obey existing scaling laws. (A) Definitions of diameters and branch length. (B) Scaled diameters (d/\bar{d} , where \bar{d} is the mean diameter of the branch) plotted against scaled position along the branch (x/l , where l is the total length of the branch). Two branches were selected for each branch order between 0 and 34 for six neurons from six 132-h larvae. The number of diameter measurements from each neuron ranged from 90 to 204. The black dashed line represents the linear regression with slope -0.023 ± 0.013 ($\pm SE$, $P = 0.078$; t test, not significant at the 95% confidence level). The left and right magenta filled circles are the mean diameters of the mothers and the daughters, respectively. (C) Histogram of values of the exponent p for 253 dendrite branch points from the six 132-h larvae. The average exponent is 7.2, and the SD is 8.8. Inset shows an enlarged view with magenta filled circles, indicating exponents predicted by the Rall, da Vinci, and Murray scaling laws.

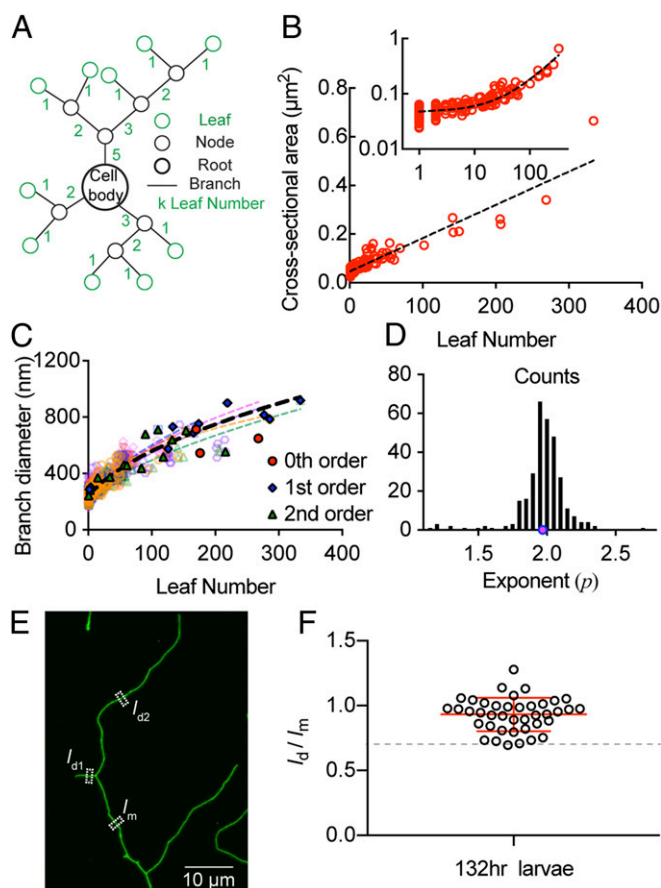


Fig. 3. Scaling of bifurcating dendrites. (A) Definition of the leaf number of a bifurcating tree. (B) Cross-sectional area vs. leaf number for one 132-h larva. Black dashed line indicates linear regression with slope $\beta = 1.36 \pm 0.03 \times 10^3 \text{ nm}^2$ and y-intercept $4.6 \pm 0.1 \times 10^4 \text{ nm}^2$. (B, Inset) Log-log plot. (C) Branch diameter vs. leaf number for six 132-h larvae. The colored dashed curves indicate the nonlinear fits to $d^p = \bar{p}n + d_0^p$ for each neuron. The black dashed curve shows fitting for all data points: $p = 2.05 \pm 0.06$, $d_0 = 240 \pm 3 \text{ nm}$ ($\pm \text{SE}$; 1,389 data points). Filled symbols indicate zeroth, first, and second branch orders, where the zeroth-order branch originates in the cell body. (D) Histogram shows the distribution of values of the exponent p fitted from: $d_m^p + d_0^p = d_{d1}^p + d_{d2}^p$ for 303 neuron branch points from six 132-h larvae. The average exponent value, denoted by a magenta circle, is 1.97 ± 0.17 ($\pm \text{SD}$). (E) Maximum projection image of a bifurcation that has two terminal, daughter branches labeled. The white boxed regions with lateral width $1.1 \mu\text{m}$ indicate the regions of dendrite where the overall intensity $I_m(I_{d1}, I_{d2})$ for mother and daughters branches of 132-h larva were obtained. (F) Intensity ratios of terminal daughters to the mother for 20 bifurcations from four 132-h larvae. Red lines 0.93 ± 0.13 indicate mean and SD.

agreement validates our SDC superresolution method and shows that the average terminal diameter is on the order of 200 nm.

Scaling Is Invariant over Development. Class IV neurons grow throughout larval development from a cell breadth of $\sim 60 \mu\text{m}$ at 24 h to $\sim 400 \mu\text{m}$ at 132 h (SI Appendix, Fig. S6). To complete the description of allometric scaling, we applied our scaling relation $d^p = \bar{p}n + d_0^p$ over all stages of development. Fig. 4 shows that the scaling parameters are roughly constant throughout development. The average value over developmental time of the exponent p is 2.40 ± 0.80 , (mean $\pm \text{SD}$, 31 larvae), corresponding approximately to area scaling (Fig. 4A). The average value over developmental time of the cross-sectional area per leaf is $1,980 \pm 685 \text{ nm}^2$ ($\pm \text{SD}$, 31 larvae) (Fig. 4B). The average value of the terminal diameter ($d_1 = (d_0^p + \bar{p})^{1/p}$) is $235 \pm 14 \text{ nm}$ ($\pm \text{SD}$, 31 larvae) (Fig. 4C) and

is independent of developmental time (SI Appendix, Fig. S7). Thus, the scaling law holds throughout the development of class IV cells. While there is substantial variability in the exponent over larval development, the exponent is more tightly centered around $p = 2$ in the older larvae (Fig. 4A); this tightening of the distribution is evidence for a maturation process that adjusts diameters over development.

Discussion

Our data show that scaling laws of the form Eq. 1, which includes Rall's law, do not hold for *Drosophila* class IV neurons: There is no one exponent that accounts for diameter changes across all bifurcations. The reason for the variability in exponents is that the branches in class IV cells have a minimum diameter, according to Eq. 2, so that the daughters in more distal branches have similar diameters to their mothers. Equal mother–daughter diameters correspond to an infinite exponent. For more proximal dendrites, by contrast, we found that the exponent approaches two. As a consequence, there is a broad range of exponents, the great majority of which exceed the Rall exponent of $3/2$. This finding agrees with studies in crustacean somatogastric ganglion neurons (14) and mammalian dendrites and axons (11, 23), in which the exponents varied from 0.5 to 4 (95% range), with medians between 2 and 3.

The deviation from Rall's law has potential functional consequences. If we assume that electrical signals propagate passively in the dendrites of class IV cells and that the decrement in signal amplitude across each branch point is minimized (12), then the larger diameters of daughters than predicted by Rall's law must be compensated for by an increase in membrane conductance (i.e., higher ion-channel density) in the daughters (SI Appendix). If electrical signals propagate actively and the propagation time across branch points is minimized, a similar compensation is required. Thus, the failure of the earlier scaling laws, and, in particular, Rall's law, suggests that there may be a trade-off between cell geometry and molecular localization.

The class IV diameter data fit the modified scaling law (Eq. 2 with $p \approx 2$): The area increases in proportion to the increase in the number of dendrite tips, and there is a minimum diameter of terminal branches. The extra cross-sectional area per tip is $2,000 \text{ nm}^2$. The average terminal diameter is 230 nm, measured by SDC microscopy, and 195 nm by SIM. These values are similar to those obtained by electron microscopy, where the finest dendrites ranged in diameter from 130 to 240 nm [figure 2 in Han et al. (16)], though chemical fixation can lead to shrinkage of $\sim 20\%$.

We hypothesize that our modified scaling law arises from cell biological and developmental constraints. The increase in cross-sectional area ($p = 2$) with dendritic tip number is consistent with dendritic tips making the major nutritional and energetic demands on the dendrite, as expected if the primary mechanism by which dendrites grow is through tip extension (24). If nutrient demand is proportional to the number of tips, and the velocity of intracellular transport is independent of dendrite diameter, as expected if motor-driven transport has a constant speed, then the nutrient supply would be proportional to the cross-sectional area. The very small amount of tapering observed over branch lengths is also consistent with the branches themselves having a low metabolic demand. The extra cross-sectional area per tip of $2,000 \text{ nm}^2$ is similar to the area occupied by one microtubule and a 30-nm vesicle carried along it by a motor protein (an ellipsoid with axes 35 and 70 nm) (Fig. 5). A similar calculation estimates the minimum diameter of axons (25). Thus, our measured area increment is consistent with the requirement that each additional tip be served by a microtubule.

A proportionality between cross-section area and number of synapses was found for foveal cone axons of adult monkey and bipolar axons in cat retina (26), suggesting that an additional microtubule may be required to convey materials toward and away from each synapse in photoreceptors. Sensory dendrites of class IV cells have no synapses. Instead input comes from the

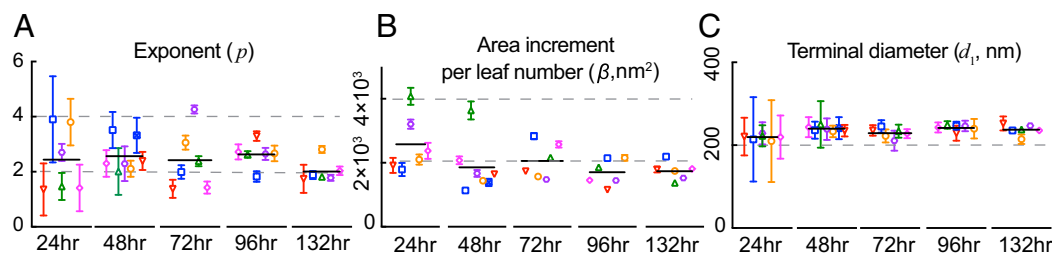


Fig. 4. The modified scaling law holds at different developmental stages. Scaling exponent, p (A), area increment per leaf, β (B), and terminal diameter, d_t (C) measured at different developmental stages (hours after egg lay). Symbols indicate means, and vertical lines indicate SEs obtained from fits to six or seven individual cells at each stage of $d_t^p = \beta + d_0^p$. Black lines denote averages.

environment. In this case, the growing dendrite tips, which are highly dynamic structures that alternate between growing and shrinking phases, may constitute the primary metabolic demand. Thus, diameter scaling may be a consequence of the metabolic needs of the cells, supporting the view that energetics is an important design consideration in the nervous system (27).

One way to interpret the minimum cross-sectional area is that each branch requires this minimum area for “housekeeping” functions. Such functions include reinforcement of the plasma membrane by the submembranous cortex, which contains actin and other proteins and can be ~ 100 -nm thick (28). Only the cross-sectional area above this minimum area is available to supply the dendritic tips. In the wide, proximal dendrites, the minimum area is small compared to the total area, whereas in the narrow, terminal dendrites, most of the cross-section is taken up by this minimum area.

An interesting consequence of terminal dendrites having a minimum diameter is that it sets a lower bound on the force required for dendrite growth. To extend a tube of membrane from a low-curvature bilayer, a force, f , is required to bend the membrane into a cylinder: $f = 4\pi\kappa/d$, where κ is the bending stiffness and d is the cylinder’s diameter (29). Therefore, the smaller the diameter, the larger the force. For a membrane stiffness of 40 pN/nm (30), extension of a tip with an average diameter of 230 nm requires a force of ~ 2 pN. A terminal diameter of 180 nm, at the lower end of the measured diameters, would require a force of 3 pN. The force will be even higher if other structures, such as internal membranes or cytoskeleton, also resist dendrite extension. This extension force is similar to the force generated by a single growing microtubule (31) or a single microtubule-based motor (32), which could drive microtubule sliding (33). While terminal dendrites in class IV cells can contain microtubules, as evidenced by EB1 comets (34), there are examples of narrow terminal dendrites that contain no microtubules, both in class IV cells and in the fly central nervous system (35, 36). Therefore, extension may be driven by other processes, such as actin polymerization (37). Dendrites have similar diameters to actin-rich filopodia (38), which can generate protrusive forces up to a few piconewtons (39). Thus, dendrite

formation could be driven by microtubules or actin filaments, or their associated motor proteins. Irrespective of the molecular mechanism, terminal dendrites with the observed diameters are easier to build than narrower ones: They could be extended by a single motor or filament, whereas much narrower dendrites would require the concerted action of multiple motors and/or filaments.

Although these arguments are conjectural, they demonstrate the plausibility that dendrite geometry is limited by cell biological constraints. This is consistent with the argument of ref. 26 that the higher calibers of cone axons compared to rod axons are not to minimize the decrement of graded signals or to quicken their electrotonic spread, but, rather, to support the larger number of microtubules that service the larger number of synapses in the cones. In class IV dendrites, we propose that the scaling of cross-sectional areas supports microtubules that service the growing dendritic tips by providing the materials and possibly forces necessary for dendrite growth (40, 41). Taken together, our data and analysis support Cajal’s conjecture that “all of the morphological features displayed by neurons appear to obey precise rules (e.g. scaling laws) that are accompanied by useful consequences (e.g. optimizing transport required for growth)” (42). Our modified scaling law may generalize to other dendrites, where we postulate that synapses impose the dominant metabolic demand. If the law generalizes, it is expected to facilitate segmentation in connectomic studies (43–45) because knowing the rules for dendrite morphology will provide priors that constrain connectomic maps, just as Ramachandran plots constrain and validate protein structures.

Materials and Methods

Drosophila melanogaster Strains. The Shibire strain *Shi^{ts1}; ppk-CD4-tdGFP* was provided by Fernando Vonnhoff (Department of Biological Science, University of Maryland, Baltimore County). *Shi^{ts1}* is a temperature-sensitive mutation that immobilizes the larva when the temperature is raised from 25.0 °C (the permissive temperature) to 30.5 °C (the nonpermissive temperature). These mutants have normal development (SI Appendix, Fig. S8) and normal nociceptive responses (SI Appendix, Fig. S9) at the permissive temperature.

The fly strain used for structure illumination imaging was *ppk-cd4-tdGFP* (a gift from Han Chun, Cornell University, Ithaca, NY).

Light-Avoidance Assay. To demonstrate that the Shibire strain has similar nociceptive response to control strains (*ppk-CD4-tdGFP*), we performed light-avoidance tests for both strains. Third-instar larvae were gently picked up from the vial and placed on a glass slide. Light was delivered by a 488-nm laser delivered into the SDC microscope through a 4 \times , NA-0.2 objective, yielding a light spot of 4 mm \times 4 mm and 0.22 mW/mm² (high intensity for larvae). An example of light avoidance is shown in SI Appendix, Fig. S9A. The imaging light was long-pass-filtered (larvae are insensitive to moderate-intensity red light). An avoidance response was scored when the animal stopped forward movement or turned its head away from the light spot. The percentage of positive responses was calculated and is shown in SI Appendix, Fig. S9B.

SDC Imaging. Embryos were collected for 2 h on apple juice agar plates with a dollop of yeast paste and aged at 25 °C in a moist chamber. The plates containing the first batch of embryos were discarded, as the dendrite morphology of class IV neurons is less consistent in those animals (16). Larvae were

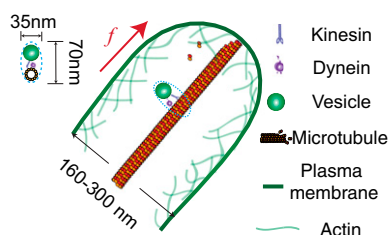


Fig. 5. Size of a dendrite tip relative to the cytoskeleton and motors. Tip of a class IV neuron with a microtubule is shown. Each microtubule and vesicle occupy a cross-sectional area of $\sim 35 \times 75$ nm², corresponding to the incremental area per leaf. The microtubule has diameter 25 nm.

immobilized individually on agarose pads (thickness 0.3 to 0.5 mm) sandwiched between a slide and a coverslip. The imaging was done by using a spinning-disk microscope: the Yokogawa CSU-W1 disk (pinhole size 50 μm) built on a fully automated Nikon TI inverted microscope with perfect focus system, a scientific complementary metal-oxide semiconductor (sCMOS) camera (Zyla 4.2 plus sCMOS), and running Nikon Elements software. The Shibire larvae were paralyzed at 30.5 $^{\circ}\text{C}$ during imaging. Individual neuron image stacks used for superresolution measurements were acquired with a 60 \times , 1.2-NA water-immersion lens with a z-step size of 0.16 μm . The whole-larva images were acquired with a 4 \times , 0.2-NA objective. To ensure that the neuronal morphology was not altered at the nonpermissive temperature, each image-acquisition process was completed within 20 min. Class IV neurons in A3–A5 segments from six or seven larvae were collected at each developmental stage.

Synthetic Image Construction. We simulated the images obtained by our SDC microscope using the following four components (46, 47): 1) model object $I(x)$ —the fluorophores randomly distributed on a cylinder surface, with pixel size 9 nm. The fluorophore density, on the order of 1,000 μm^{-2} , was based on estimations of the single-fluorophore intensity in the spinning-disk microscope. 2) Illumination field $I(x)$ —the light intensity as a function of position. The illumination field is described as a product of an x – y illumination and a z modulation: $I(x) = I_{xy}(x, y) \times I_z(z)$. In practice, aberrations due to refractive-index mismatches cause a dimming of the illumination with depth into the sample (48). Since this overall dimming only depends on the depth z from the interface, and not on the x – y position in the sample, it is natural to describe the illumination field as a product of a uniform x – y illumination and a z modulation. 3) PSF $P_{\text{conf}}(x, x')$ —the image of an individual fluorophore due to diffraction of light—was based on the Gibson and Lanni scalar model (49, 50); it gave similar results to the vectorial-based PSF model (51). The pinhole size of the confocal microscope (50 μm) was also incorporated into $P_{\text{conf}}(x, x')$ (52, 53). 4) Image noise $B(x)$ —autofluorescent signal from the surrounding environment. These components were combined to form the simulated image through convolution: $M(x) = B(x) + \int d^3x' I(x') P_{\text{conf}}(x - x'; x)$, which was sampled at discrete pixel locations to get the final simulated image $M(x)$ (in units of photon number). These photons were then transformed into a number of electrons based on quantum efficiency, shot noise, and the sCMOS parameters. Then, the image was reduced to the desired camera resolution—for example, 108 nm/pixel. These values were fed to an electron-to-digital number converter (considering the readout noise) to obtain synthetic images (47) (SI Appendix, Fig. S2).

Superresolution Method Based on MC Optimization. The superresolution method generated simulated images $M(x)$ without photon shot noise. The tunable parameters of the optimization are the diameter of the model cylinder, cylinder orientation and position, the FWHM of the PSF (x – y plane) determined from sample refractive index (1.33 to 1.55), pinhole diameter (1.6 to 2.5 Airy Unit), emission wavelength (500 to 550 nm), and amplitude of the spatially uniform background (<https://github.com/Maijia-cpu/Super-resolution-Method>). The fluorophore density 1,646/ μm^2 in the model was chosen based on estimations from the absolute intensity of the experimental images. At each step, a simulated image was generated based on the tuned parameters. Then, a comparison between the simulated image and the experimental image was made. The MC optimization aimed to find the diameter that minimized the square of the difference (54):

$$D = \sum_{m=0}^I \frac{\sum_{j=0}^N (I_{\text{exp}}^{mj} - I_{\text{sim}}^{mj})^2 A_{\text{exp}}^m}{N \sum_{m=0}^I A_{\text{exp}}^m},$$

where I_{sim}^{mj} stands for intensity profile across the cylinder as a function of pixel number j and image section m of the stack, N stands for the total number of pixels for image section m , and A^m stands for total pixel intensity of image section m . Subscript exp stands for experimental images, while sim stands for simulated images. Six 1,000-step simulations were carried out for each branch diameter detection. Averages were made over three model cylinder orientations: 0.0, 0.5, and 1.0 radians relative to the axial direction. Each simulation gives the diameter that minimizes the square of the difference. The inferred diameter is an average of diameters from six simulations.

Tetra-Speck Beads Measurements. We used tetra-speck beads of diameter 100 nm (Invitrogen, catalog no. T7279) for PSF FWHM characterizations. The bead stock solution was diluted 100-fold ratio into BRB80 buffer with 0.2M KCl and then flowed into a flow channel made by parafilm. The sample was imaged by using the same objective (60 \times , 1.2-NA water-immersion lens) used for imaging larvae. The image resolution was 108 nm/pixel. To extract the PSF

from 100-nm diameter tetra-speck beads images, we modeled a 100-nm bead, convolved it with a tunable PSF, and then fit it to the bead images of the central part. The MC optimization was used to find the PSF that minimized the square of the intensity difference. The results are shown in Fig. 1F. The PSF FWHM shown in Fig. 1E and F was measured with PSF resolution 9 nm/pixel.

Method for Obtaining Reconstructed SIM Images. The larvae were mounted in 50% glycerol in phosphate-buffered saline between a glass slide and a coverslip. The raw images of the class IV neurons were collected by using a DeltaVision OMX superresolution imaging system (GE Healthcare) equipped with a monochrome sCMOS camera (PCO edge) and a 60 \times Plan Apo oil objective (NA 1.42) (Olympus). The raw images were then reconstructed and deconvolved by using the DeltaVision software (GE Healthcare) to obtain three-dimensional SIM images.

Estimation of Diameters from SIM Images. The SIM images are deconvolved and show “ringing” at the dendrite edges consistent with a Wiener-type deconvolution. To estimate the diameter from these images, we used MC optimization with the four tuning parameters: cylinder diameter, FWHM of Gaussian-approximated PSF, Wiener filter constant, and slab thickness of the central part of the image (more details can be found in SI Appendix). At each step, a simulated image was generated based on the tuning parameters. Then, a comparison between the simulated image and the experimental image was made. MC optimization also aimed to minimize the squared difference $D = \sum_{j=1}^N (I_{\text{sim}} - I_{\text{exp}})^2$, where I stands for intensity profile across the cylinder as a function of pixel number j . Subscript exp stands for experimental images, while sim stands for simulated images. A more detailed description can be found in SI Appendix.

Class IV Dendrite Tracing. To quantify dendrite morphology, z-series images for a given neuron were projected onto a two-dimensional image file, and dendrite arbors were traced by tree toolbox software (55). To improve accuracy, the traces were further adjusted based on intensity profiles from maximum-intensity-projection images. Leaf number, branch order, and Strahler number (SI Appendix, Fig. S3) were measured from the traces.

Criteria for Selecting Dendrite Branches for Superresolution Analysis. Our superresolution method aims to find diameters of hollow cylinders that best fit dendrite branches. We analyzed branches longer than 5 μm . We avoided regions containing endoplasmic reticulum (ER) or Golgi apparatus (examples can be found in Fig. 1 and SI Appendix, Fig. S10) (56). Some zeroth-order branches (connected to the soma) are rich in organelles and were not considered for this reason. These regions have higher intensities or larger diameters. Outliers of maximum intensity values and FWHM along the dendrite branches were first identified. The corresponding parts of branches were then removed. The remaining parts of the branches were then used for further analysis.

Scaled Diameters and Positions. After removing the parts of a branch that contain ER or Golgi apparatus, the remaining parts of that branch can be discontinuous. Through combining all remaining parts of the branch as a whole, we obtained a “new” branch with all the above criteria satisfied. Then, three positions were chosen at 1/3, 1/2, and 2/3 of the newly constructed branch, and branch diameters were calculated at corresponding positions. The distance between the selected positions and the branch point nearest the soma in the original branch geometry is denoted as x_i ($i = 1, 2, 3$). Mean diameter of each branch denoted by \bar{d} is an average of d_i ($i = 1, 2, 3$).

Exponent p Measurements. Previous scaling laws have the form: $d_m^p = d_{d1}^p + d_{d2}^p$. The exponent p is estimated by minimizing the difference between the right- and left-hand sides of the equation. To determine this value, we used the function fsolve in MATLAB.

Data Availability. Detailed materials and methods are reported in SI Appendix. The code to perform MC simulation is available on GitHub (<https://github.com/Maijia-cpu/Super-resolution-Method>). Raw images are available on Dryad (doi:10.5061/dryad.wstjq2mp).

ACKNOWLEDGMENTS. We thank members of the J.H. laboratory for comments on an earlier draft. We benefited from discussions with Yuhai Tu (IBM Watson Laboratory) and J.H. laboratory members during the execution of this work and comments on the manuscript from Rob Phillips. This study was supported by NIH Grants DP1 MH110065 and R01 NS118884.

1. P. Ball, *Branches: Nature's Patterns: A Tapestry in Three Parts* (Oxford University Press, Oxford, UK, 2009).
2. A. Rinaldo, R. Rigon, J. R. Banavar, A. Maritan, I. Rodriguez-Iturbe, Evolution and selection of river networks: Statics, dynamics, and complexity. *Proc. Natl. Acad. Sci. U.S.A.* **111**, 2417–2424 (2014).
3. G. B. West, J. H. Brown, Life's universal scaling laws. *Phys. Today* **57**, 36–43 (2004).
4. S. M. Rafelski et al., Mitochondrial network size scaling in budding yeast. *Science* **338**, 822–824 (2012).
5. D. A. Fletcher, R. D. Mullins, Cell mechanics and the cytoskeleton. *Nature* **463**, 485–492 (2010).
6. J. R. Banavar, A. Maritan, A. Rinaldo, Size and form in efficient transportation networks. *Nature* **399**, 130–132 (1999).
7. C. D. Murray, The physiological principle of minimum work: I. The vascular system and the cost of blood volume. *Proc. Natl. Acad. Sci. U.S.A.* **12**, 207–214 (1926).
8. A. Bejan, J. P. Zane, *Design in Nature: How the Constructal Law Governs Evolution in Biology, Physics, Technology, and Social Organizations* (Anchor, New York, 2013).
9. J. P. Richter, *The Notebooks of Leonardo da Vinci* (Dover Publications, New York, 1970).
10. W. Rall, Branching dendritic trees and motoneuron membrane resistivity. *Exp. Neurol.* **1**, 491–527 (1959).
11. D. B. Chklovskii, A. Stepanyants, Power-law for axon diameters at branch point. *BMC Neurosci.* **4**, 18 (2003).
12. Q. Wen, D. B. Chklovskii, A cost-benefit analysis of neuronal morphology. *J. Neurophysiol.* **99**, 2320–2328 (2008).
13. K. Shinozaki, K. Yoda, K. Hozumi, T. Kira, A quantitative analysis of plant form: the pipe model theory: I. Basic analyses. *Jap. J. Ecol.* **14**, 97–105 (1964).
14. A. G. Otopalik et al., Sloppy morphological tuning in identified neurons of the crustacean stomatogastric ganglion. *eLife* **6**, e22352 (2017).
15. Y.-N. Jan, L. Y. Jan, Branching out: Mechanisms of dendritic arborization. *Nat. Rev. Neurosci.* **11**, 316–328 (2010).
16. C. Han et al., Integrins regulate repulsion-mediated dendritic patterning of *Drosophila* sensory neurons by restricting dendrites in a 2D space. *Neuron* **73**, 64–78 (2012).
17. W. B. Grueber, L. Y. Jan, Y. N. Jan, Tiling of the *Drosophila* epidermis by multidendritic sensory neurons. *Development* **129**, 2867–2878 (2002).
18. R. Y. Hwang et al., Nociceptive neurons protect *Drosophila* larvae from parasitoid wasps. *Curr. Biol.* **17**, 2105–2116 (2007).
19. W. Song, M. Onishi, L. Y. Jan, Y. N. Jan, Peripheral multidendritic sensory neurons are necessary for rhythmic locomotion behavior in *Drosophila* larvae. *Proc. Natl. Acad. Sci. U.S.A.* **104**, 5199–5204 (2007).
20. W. B. Grueber et al., Projections of *Drosophila* multidendritic neurons in the central nervous system: Links with peripheral dendrite morphology. *Development* **134**, 55–64 (2007).
21. G. S. Kassab, Y.-C. B. Fung, The pattern of coronary arteriolar bifurcations and the uniform shear hypothesis. *Ann. Biomed. Eng.* **23**, 13–20 (1995).
22. M. Zamir, J. A. Medeiros, Arterial branching in man and monkey. *J. Gen. Physiol.* **79**, 353–360 (1982).
23. C. Cherniak, M. Changizi, D. Kang, Large-scale optimization of neuron arbors. *Phys. Rev. E Stat. Phys. Plasmas Fluids Relat. Interdiscip. Topics* **59** (5 Pt B), 6001–6009 (1999).
24. F. B. Gao, J. E. Brenman, L. Y. Jan, Y. N. Jan, Genes regulating dendritic outgrowth, branching, and routing in *Drosophila*. *Genes Dev.* **13**, 2549–2561 (1999).
25. A. A. Faisal, J. A. White, S. B. Laughlin, Ion-channel noise places limits on the miniaturization of the brain's wiring. *Curr. Biol.* **15**, 1143–1149 (2005).
26. A. Hsu, Y. Tsukamoto, R. G. Smith, P. Sterling, Functional architecture of primate cone and rod axons. *Vision Res.* **38**, 2539–2549 (1998).
27. P. Sterling, S. Laughlin, *Principles of Neural Design* (MIT Press, Cambridge, MA, 2015).
28. P. Chugh, E. K. Paluch, The actin cortex at a glance. *J. Cell Sci.* **131**, jcs186254 (2018).
29. I. Derényi, F. Jülicher, J. Prost, Formation and interaction of membrane tubes. *Phys. Rev. Lett.* **88**, 238101 (2002).
30. M. M. Kamal, D. Mills, M. Grzybek, J. Howard, Measurement of the membrane curvature preference of phospholipids reveals only weak coupling between lipid shape and leaflet curvature. *Proc. Natl. Acad. Sci. U.S.A.* **106**, 22245–22250 (2009).
31. M. Dogterom, B. Yurke, Measurement of the force-velocity relation for growing microtubules. *Science* **278**, 856–860 (1997).
32. J. Howard, *Mechanics of Motor Proteins and the Cytoskeleton* (Sinauer Associates, Sunderland, MA, 2001).
33. W. Lu, P. Fox, M. Lakonishok, M. W. Davidson, V. I. Gelfand, Initial neurite outgrowth in *Drosophila* neurons is driven by kinesin-powered microtubule sliding. *Curr. Biol.* **23**, 1018–1023 (2013).
34. K. M. Ori-McKenney, L. Y. Jan, Y.-N. Jan, Golgi outposts shape dendrite morphology by functioning as sites of acentrosomal microtubule nucleation in neurons. *Neuron* **76**, 921–930 (2012).
35. S. Nanda, S. Bhattacharjee, D. N. Cox, G. A. Ascoli, Distinct relations of microtubules and actin filaments with dendritic architecture. *iScience* **23**, 101865 (2020).
36. C. M. Schneider-Mizell et al., Quantitative neuroanatomy for connectomics in *Drosophila*. *eLife* **5**, e12059 (2016).
37. V. Nithianandam, C.-T. Chien, Actin blobs prefigure dendrite branching sites. *J. Cell Biol.* **217**, 3731–3746 (2018).
38. P. K. Mattila, P. Lappalainen, Filopodia: Molecular architecture and cellular functions. *Nat. Rev. Mol. Cell Biol.* **9**, 446–454 (2008).
39. D. Cojoc et al., Properties of the force exerted by filopodia and lamellipodia and the involvement of cytoskeletal components. *PLoS One* **2**, e1072 (2007).
40. P. W. Baas, A. N. Rao, A. J. Matamoros, L. Leo, Stability properties of neuronal microtubules. *Cytoskeleton (Hoboken)* **73**, 442–460 (2016).
41. L. C. Kapitein, C. C. Hoogenraad, Building the neuronal microtubule cytoskeleton. *Neuron* **87**, 492–506 (2015).
42. S. R. Cajal, *Histology of the Nervous System of Man and Vertebrates* (Oxford University Press, New York, 1995), vol. 6.
43. S. Seung, *Connectome: How the Brain's Wiring Makes Us Who We Are* (Houghton Mifflin Harcourt, Boston, MA, 2012).
44. Y. Wang, A. Gupta, M. Toledo-Rodriguez, C. Z. Wu, H. Markram, Anatomical, physiological, molecular and circuit properties of nest basket cells in the developing somatosensory cortex. *Cereb. Cortex* **12**, 395–410 (2002).
45. C. S. Xu et al., A connectome of the adult *Drosophila* central brain. *BioRxiv* [Preprint] (2020). <https://doi.org/10.1101/2020.01.21.911859> (Accessed January 1, 2021).
46. M. Bierbaum, B. D. Leahy, A. A. Alemi, I. Cohen, J. P. Sethna, Light microscopy at maximal precision. *Phys. Rev. X* **7**, 041007 (2017).
47. D. Sage et al., Quantitative evaluation of software packages for single-molecule localization microscopy. *Nat. Methods* **12**, 717–724 (2015).
48. S. Hell, G. Reiner, C. Cremer, E. H. Stelzer, Aberrations in confocal fluorescence microscopy induced by mismatches in refractive index. *J. Microsc.* **169**, 391–405 (1993).
49. S. F. Gibson, F. Lanni, Experimental test of an analytical model of aberration in an oil-immersion objective lens used in three-dimensional light microscopy. *J. Opt. Soc. Am. A* **9**, 154–166 (1992).
50. J. Li, F. Xue, T. Blu, Fast and accurate three-dimensional point spread function computation for fluorescence microscopy. *J. Opt. Soc. Am. A Opt. Image Sci. Vis.* **34**, 1029–1034 (2017).
51. B. Richards, E. Wolf, Electromagnetic diffraction in optical systems, II. Structure of the image field in an aplanatic system. *Proc. R. Soc. Lond. A Math. Phys. Sci.* **253**, 358–379 (1959).
52. S. Kimura, T. Wilson, Effect of axial pinhole displacement in confocal microscopes. *Appl. Opt.* **32**, 2257–2261 (1993).
53. T. Wilson, C. Sheppard, *Theory and Practice of Scanning Optical Microscopy* (Academic Press, London, 1984).
54. F. Flicker, J. van Wezel, Charge order in NbSe₂. *Phys. Rev. B* **94**, 235135 (2016).
55. H. Cuntz, F. Forstner, A. Borst, M. Häusser, One rule to grow them all: A general theory of neuronal branching and its practical application. *PLOS Comput. Biol.* **6**, e1000877 (2010).
56. M. M. Corty, B. J. Matthews, W. B. Grueber, Molecules and mechanisms of dendrite development in *Drosophila*. *Development* **136**, 1049–1061 (2009).